

Spectroscopic Studies of Transition Metal Complexes

by

QIAOQIAO XIE

A Dissertation submitted to the

Graduate School-Newark

Rutgers, The State University of New Jersey

In partial fulfillment of the requirements

For the degree of

Master of Science

Graduate Program in Department of Chemistry

Written under the direction of

Professor Jenny Lockard

And approved by

Newark, New Jersey

October, 2017



@2017

Qiaoqiao Xie

ALL RIGHTS RESERVED

Table of Contents

ABSTRACT	II
LIST OF FIGURES	IV
LIST OF TABLES	VI
CHAPTER ONE	
RESONANCE RAMAN SPECTROSCOPY STUDY OF TRINUCLEAR METAL-COORDINATION COMPLEXES.....	1
1.1 Introduction.....	1
1.2 Methods.....	3
1.2.1 UV-Vis Spectroscopy	3
1.2.2 Raman Spectroscopy	4
1.3 Results	5
1.3.1 UV– Vis spectroscopy	5
1.3.2 Raman and Resonance Raman Spectroscopy	7
1.4 Discussion	14
1.5 References.....	18
CHAPTER TWO	
RESONANCE RAMAN SPECTROSCOPY STUDY OF CU(I) COMPLEXES.....	20
2.1 Introduction.....	20
2.2 Methods.....	21
2.2.1 UV-Vis Spectroscopy	21
2.2.2 Raman Spectroscopy	22

2.3 Results and Discussion.....	22
--	-----------

2.4 References.....	28
----------------------------	-----------

CHAPTER THREE

FUNDAMENTAL STUDY OF RU-S BONDING IN A SERIES OF RU-S/SO COMPLEXES	29
---	-----------

3.1 Introduction.....	29
------------------------------	-----------

3.2 Methods.....	32
-------------------------	-----------

3.2.1 XAS Data collection.....	32
--------------------------------	----

3.2.2 TD-DFT Calculations.....	32
--------------------------------	----

3.3 Results and Discussion.....	33
--	-----------

3.3.1 Me-bim-ipr (A) vs Et-bim-ipr (B):	34
---	----

3.3.2 Et-bim-ph (A) vs Et-bim-ipr (B):	36
--	----

3.4 References.....	38
----------------------------	-----------

Acknowledgements

I would like to express my sincere thanks to my supervisor, Professor Jenny Lockard, for her kindness, help, long-term support and guidance she has given me during my studies. Especially, I am thankful for her advice and patience during correcting my thesis. It has been a pleasure studying in and being a member of her research group.

I am also grateful to my committee members, Prof. Piotr Piotrowiak, Prof. Huixin He and Prof. Michele Pavanello for their help and time in correcting my thesis.

My gratitude also goes to all members of the Lockard's group, both past and present, Dr. Pavel Kucheryavy, Dr. Yuan Chen, Lauren Hanna, Nicole Lahanas and Mikhail Solovyev, for all of their assistance and teaching me all the techniques required in our lab, and for their support and motivation.

I greatly appreciate the faculty members of the Chemistry Department, Prof. John Sheridan and Prof. Rudolph Kluiber, for accepting me as a teaching assistant, their knowledge, research advice, excellent teaching and guiding me throughout my education endeavors.

I would like to take this opportunity to thank the members of the chemistry office, Judy Slocum, Monika Dabrowski, Lorraine McClendon, and also the staff of both the Department of Chemistry and Rutgers University for their helpfulness.

Last, but not the least, I would like to thank my family for always having a sympathetic and open ear when I got frustrated with my progress, even though the things I was talking about often made little sense to them.

Abstract
Spectroscopic Studies of Transition Metal Complexes

BY
QIAOQIAO XIE

Dissertation Director:
Professor Jenny Lockard

This thesis describes utilizing spectroscopy techniques, such as Resonance Raman spectroscopy and X-ray absorption spectroscopy, for some fundamental studies of transition metal complexes. Firstly, a series of Fe-Pt-Fe trinuclear complexes are investigated by resonance Raman spectroscopy. The spectroscopic studies can provide insight into the ground state and excited state of the related complexes, and help us to understand the charge ligand and conformation effect on photoinduced charge transfer. Three trinuclear complexes were compared: $[(\text{NC})_5\text{FeCN-Pt}(\text{L})_n\text{-NCFE}(\text{CN})_5]^{4+}$ (abbreviated as $[\text{Fe}_2\text{Pt}(\text{L})_2]^{4+}$), where $\text{L} = \text{NH}_3$, ($n=4$); cyclam, ($n=1$); ethylenediamine(en), ($n=2$). The crystal structures reveal that the cyclam complex has an eclipsed configuration, while the ammonia ligands yield a staggered one. The crystal structure of $[\text{Fe}_2\text{Pt}(\text{en})_2]^{4+}$ is not available, so the twist angle between the CN and en equatorial ligands is not known. By doing the Raman frequency analysis, we concluded that the eclipsed conformation allows more electronic delocalization across the Fe-CN-Pt bridge. The resonance Raman intensity analysis provides us that the largest contribution

to the vibrational barrier to electron transfer were those modes associated with the Fe-CN-Pt bridge. Comparing the Raman data of those trinuclear complexes, we assumed that the conformation of $[\text{Fe}_2\text{Pt}(\text{en})_2]^{4+}$ might be in between those of the $[\text{Fe}_2\text{Pt}(\text{NH}_3)_4]^{4+}$ and $[\text{Fe}_2\text{Pt-cyclam}]^{4+}$ complexes.

Secondly, some Copper(I) diimine coordination complexes have the ability to flatten out in the metal-to-ligand charge transfer (MLCT) state after populating through photoexcitation. This ability is crucial to the subsequent dynamics and structures present in the excited state. A series of Cu(I) complexes which have different ligand environments has been synthesized. We propose to use resonance Raman to investigate how the coupling of two Cu(I) atoms through a bridging bisphenanthroline ligand affects the nature of the MLCT excited state.

Thirdly, some ruthenium polypyridine sulfoxide complexes exhibit photochromic behavior. The photo-triggered isomerization of this kind of complex involves the transformation of sulfoxide from Ru-S to Ru-O bonded. This photo-induced isomerization dramatically changed the spectroscopic and electrochemical properties of the metal complexes. In our project, intermediate-energy X-ray absorption spectroscopy (XAS) was used to characterize the series of Ru-S/SO complexes related to their photo-isomerizable analogues. By collecting sulfur K-edge XAS data for this series of structurally similar complexes exhibiting diverse photochemical reactivity, and combining with TD-DFT calculations, an attempt was made to characterize the σ and π contributions to the HOMO correlate them with their reactivity.

List of Figures

Figure 1.1 Structures of $[\text{Fe}_2\text{Pt}(\text{NH}_3)_4]^{4+}$ (left) vs $[\text{Fe}_2\text{Pt-cyclam}]^{4+}$ (right).....	3
Figure 1.2 Structure of $[\text{Fe}_2\text{Pt}(\text{en})_2]^{4+}$	3
Figure 1.3 UV-Vis absorption spectrum of $[\text{Fe}_2\text{Pt}(\text{NH}_3)_4]^{4+}$ (black), $[\text{Fe}_2\text{Pt-cyclam}]^{4+}$ (red) and $[\text{Fe}_2\text{Pt}(\text{en})_2]^{4+}$ (blue)	6
Figure 1.4 UV-Vis spectra of $[\text{Fe}_2\text{Pt}(\text{NH}_3)_4]^{4+}$ (a), $[\text{Fe}_2\text{Pt}(\text{en})_2]^{4+}$ (b) and $[\text{Fe}_2\text{Pt-cyclam}]^{4+}$ (c) showing Gaussian fits of lowest energy band	7
Figure 1.5 Resonance Raman spectra vs Non-resonance Raman spectra of $[\text{Fe}_2\text{Pt}(\text{NH}_3)_4]^{4+}$, $[\text{Fe}_2\text{Pt}(\text{en})_2]^{4+}$, $[\text{Fe}_2\text{Pt-cyclam}]^{4+}$	9
Figure 1.6 Raman spectrum of $[\text{Fe}_2\text{Pt}(\text{NH}_3)_4]^{4+}$ (black), $[\text{Fe}_2\text{Pt}(\text{en})_2]^{4+}$ (red) and $[\text{Fe}_2\text{Pt-cyclam}]^{4+}$ (blue).....	10
Figure 1.7 Normalized excitation profiles of $[\text{Fe}_2\text{Pt}(\text{NH}_3)_4]^{4+}$	13
Figure 1.8 Normalized excitation profiles of $[\text{Fe}_2\text{Pt-cyclam}]^{4+}$	13
Figure 1.9 Normalized excitation profiles of $[\text{Fe}_2\text{Pt}(\text{en})_2]^{4+}$	14
Figure 1.10 Simplified bonding illustration of $[\text{Fe}_2\text{Pt-cyclam}]^{4+}$ (up) vs $[\text{Fe}_2\text{Pt}(\text{NH}_3)_4]^{4+}$ (down).....	16
Figure 2.1 Structures of Cu(I) complexes: (a) Cu(I)-monomer-1; (b) Cu(I)-monomer-2; (c) Cu(I)-monomer-3; (d) Cu(I)-dimer	21
Figure 2.2 UV-Vis absorption spectrum of Cu(I) complexes.....	23
Figure 2.3 Raman and resonance Raman spectra of Cu(I) dimer	23
Figure 2.4 Raman and resonance Raman spectra of Cu(I) monomer-1	24
Figure 2.5 Raman and resonance Raman spectra of Cu(I) monomer-2.....	24
Figure 2.6 Raman and resonance Raman spectra of Cu(I) monomer-3.....	25
Figure 2.7 Resonance Raman spectra of Cu(I) dimer (black), monomer-1 (red), monomer-2 (green) and monomer-3 (blue)	26
Figure 3.1 Structures of Ru-S complexes (a) me-bim- <i>i</i> pr; (b) et-bim- <i>i</i> pr; (c) et-bimSO- <i>i</i> pr; (d) et-bim-ph-R (R=H, R=MeO, R=F)	31

Figure 3.2 Experimental XAS spectrum of Ru-S/SO complexes	33
Figure 3.3 Comparison of the experimental (top) and calculated (bottom) S K-pre-edge spectra for Ru-S complexes. Calculated intensity in arbitrary units.....	34
Figure 3.4 Calculated XAS spectrum of me-bim- <i>ipr</i> (blue) and et-bim- <i>ipr</i> (red)	35
Figure 3.5 Calculated XAS spectrum of et-bim- <i>ph</i> (red) and et-bim- <i>ipr</i> (black)	36

List of Tables

Table 1.1 Raman shifts and Assignments of $[\text{Fe}_2\text{Pt}(\text{NH}_3)_4]^{4+}$, $[\text{Fe}_2\text{Pt}(\text{en})_2]^{4+}$ and $[\text{Fe}_2\text{Pt-cyclam}]^{4+}$	11
Table 1.2 Raman Data and Intensity Analysis Calculations of $[\text{Fe}_2\text{Pt}(\text{NH}_3)_4]^{4+}$, $[\text{Fe}_2\text{Pt}(\text{en})_2]^{4+}$ and $[\text{Fe}_2\text{Pt-cyclam}]^{4+}$	12
Table 2.1 Raman frequency and intensity of Cu(I) Dimer, monomer-1, monomer-2 and monomer-3	27
Table 3.1 Calculated angle and bond length of me-bim-ipr vs et-bim-ipr.....	35

Chapter One

Resonance Raman Spectroscopy Study of Trinuclear Metal-Coordination Complexes

1.1 Introduction

Photoinduced charge transfer is the most basic process behind photophysical, and photochemical behavior observed in both natural and artificial system.¹⁻⁴ Charge transfer can occur between the molecules with different electron affinities and ionization potentials, and also between different donor and acceptor groups within the same molecule. Given their fundamental nature, intramolecular and intermolecular charge transfer processes have been the subject of intense study for many years.⁵⁻⁶ Spectroscopic studies can provide insight into the ground state and excited state of these systems, and help us improve our understanding of charge transfer processes.⁷

Multi-nuclear transition metal complexes have been crucial in experimental studies used to develop our understanding of electron transfer processes.⁸ Bocarsly et al. reported the synthesis of a trinuclear mixed valence complex $[(\text{NC})_5\text{FeCN-Pt}(\text{NH}_3)_4\text{NC-Fe}(\text{CN})_5]^{4-}$ as shown in Figure 1.1 (left).³ This complex undergoes a one electron photoinduced metal-to-metal charge transfer, MMCT transition from one Fe(II) donor site to the Pt(IV) center. While the presence of the other iron site affords a possible second electron

transfer, important insights can be gained on these types of multinuclear electron transfer systems through the study of the one electron MMCT state. This complex was investigated using a simple time-dependent resonance Raman intensity analysis devised by Heller et al.⁹ With this intensity analysis, the relative coordinate displacements can be obtained, which provides insight on excited state structure changes.¹⁰

Recently, our collaborator Dr. Brian Pfennig from Ursinus College, synthesized another trinuclear mixed valence complex with cyclam (1, 4, 8, 11-tetraazacyclotetradecane) instead of the ammonia ligands: $[(\text{NC})_5\text{FeCN-Pt}(\text{cyclam})\text{NC-Fe}(\text{CN})_5]^{4-}$. This complex undergoes the analogous photoinduced metal-to-metal charge transfer (MMCT) transition as the one with NH_3 ligands. We found that by comparing the crystal structures of $[\text{Fe}_2\text{Pt-cyclam}]^{4-}$ and $[\text{Fe}_2\text{Pt}(\text{NH}_3)_4]^{4-}$, the Pt-N bonds are more in line with the Fe-CN bonds in $[\text{Fe}_2\text{Pt-cyclam}]^{4-}$, leading to an eclipsed configuration, while in $[\text{Fe}_2\text{Pt}(\text{NH}_3)_4]^{4-}$, they are staggered (see Figure 1.1). A related trinuclear complex, with ethylenediamine (en) ligands on the Pt (IV) (see Figure 1.2) was also synthesized; however, a crystal structure of this complex is not available. Therefore, the twist angle between the CN and en equatorial ligands is not known. In this project we use resonance Raman spectroscopy to investigate the differences between these ligand environments and the nature of excited state structure changes.

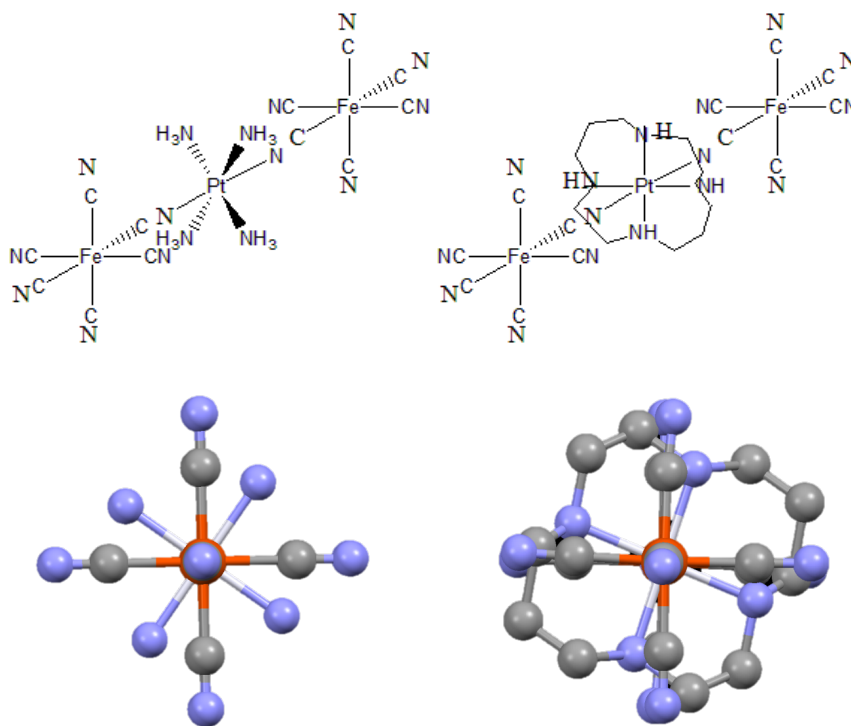


Figure 1.1 Structures of $[\text{Fe}_2\text{Pt}(\text{NH}_3)_4]^{4-}$ (left) vs $[\text{Fe}_2\text{Pt-cyclam}]^{4-}$ (right)

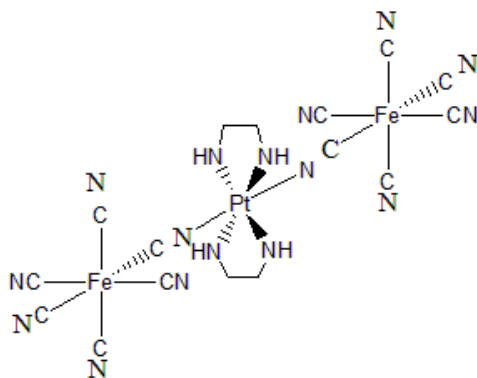


Figure 1.2 Structure of $[\text{Fe}_2\text{Pt}(\text{en})_2]^{4-}$

1.2 Methods

1.2.1 UV-Vis Spectroscopy

Ultraviolet-visible spectroscopy refers to absorption spectroscopy in the ultraviolet-visible spectral region. UV-vis spectra of the samples were obtained in the aqueous

solution containing 5 mM of each complex, in a quartz cuvette with 10 mm pathlength, using a Cary-Varian UV-visible-NIR spectrophotometer.

1.2.2 Raman Spectroscopy

Normal Raman measurements were collected using a 785 nm single-frequency diode laser with ~25 mW power. Resonance Raman spectra were collected using 532 nm and 561 nm single-frequency solid state lasers and the output of a tunable picosecond Ti: Sapphire oscillator laser was used to generate 400 nm- 500 nm excitation wavelengths by second harmonic generation. Spectra were collected using a triple monochromator, and a liquid nitrogen-cooled CCD detector with a 1340×100 pixel chip (Princeton Instruments). Raman data was collected in a quartz spinning liquid cell. The sample was spun to minimize the residence time of the laser on one spot of the sample, to avoid excessive heating.

The complexes, $[\text{Fe}_2\text{Pt}(\text{NH}_3)_4][\text{Pt}(\text{NH}_3)_4]_2$, $[\text{Fe}_2\text{Pt-cyclam}][\text{Pt}(\text{cyclam})]_2$ and $[\text{Fe}_2\text{Pt}(\text{en})_2][\text{Pt}(\text{en})_2]_2$ were obtained from Brian Pfennig of Ursinus College. $[\text{Fe}_2\text{Pt}(\text{NH}_3)_4]^{4+}$ was measured with 14 mM concentration in an aqueous solution containing 0.5 M KNO_3 as an internal standard, which was used both for frequency calibration and for normalization needed for the intensity analysis. The $[\text{Fe}_2\text{Pt-cyclam}]^{4+}$ and $[\text{Fe}_2\text{Pt}(\text{en})_2]^{4+}$ were collected also with 14 mM concentration and either 0.5 M K_2SO_4 or KNO_3 as internal standard.

Resonance Raman Intensity Analysis Theory:

The resonance Raman spectrum of the trinuclear mixed valence complexes can help us to calculate the relative contributions of each resonantly enhanced vibrational mode to the internal activation barrier for the optical electron transfer process. By comparing the intensities (I) and ground state frequencies (ν) of the enhanced vibrational modes, relative coordinate displacements (Δ) can be obtained as described by Savin's formula (eq 1), where index 1 and 2 indicate any combination of arbitrary modes. Eq 2 shows how the sum of the products of the mode displacements and the ground state frequencies is related to the width of the electronic absorption spectrum, where $8\sigma^2$ is the square of the electronic absorption bandwidth at $(1/e)$ its maximum height. According to eq 2 and the electronic absorption spectra, we can obtain the absolute scaling of the coordinate displacements.¹¹ Note: this relationship is an approximation that assumes that the width of the adsorption spectrum is dominated by contributions from internal vibrational reorganization. Solvent effects and other outer sphere contributions are not included.

$$\frac{I_1}{I_2} = \frac{\Delta_1^2 \nu_1^2}{\Delta_2^2 \nu_2^2} \quad (1)$$

$$2\sigma^2 = \sum_k \Delta_k^2 \nu_k^2 \quad (2)$$

1.3 Results

1.3.1 UV- Vis spectroscopy

The UV-Vis absorption spectra of the three trinuclear complexes are shown in Figure 1.3. The major bands (with peak maxima ranging from 420 nm to 462 nm) in the figure were assigned as photoinduced electron transfer from Fe \rightarrow Pt (MMCT). In order to find the

width at the 1/e of the maximum height, then to scale the relative displacements (Δ), we fitted the absorption spectrum with Gaussian function, see Figure 1.4.

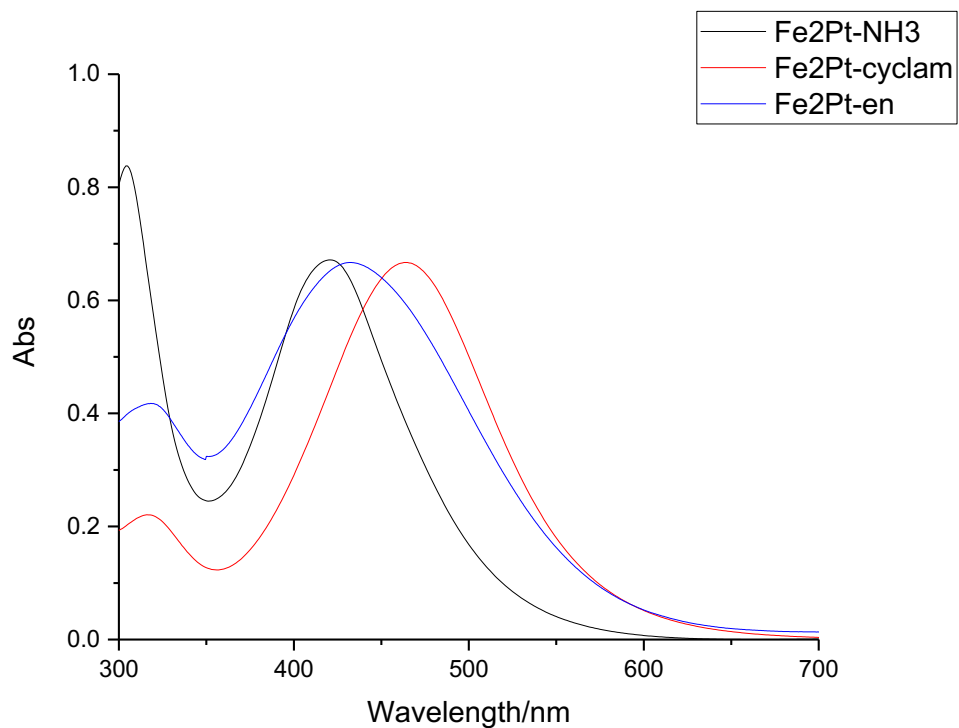


Figure 1.3 UV-Vis absorption spectrum of $[\text{Fe}_2\text{Pt}(\text{NH}_3)_4]^{4+}$ (black), $[\text{Fe}_2\text{Pt-cyclam}]^{4+}$ (red) and $[\text{Fe}_2\text{Pt}(\text{en})_2]^{4+}$ (blue)

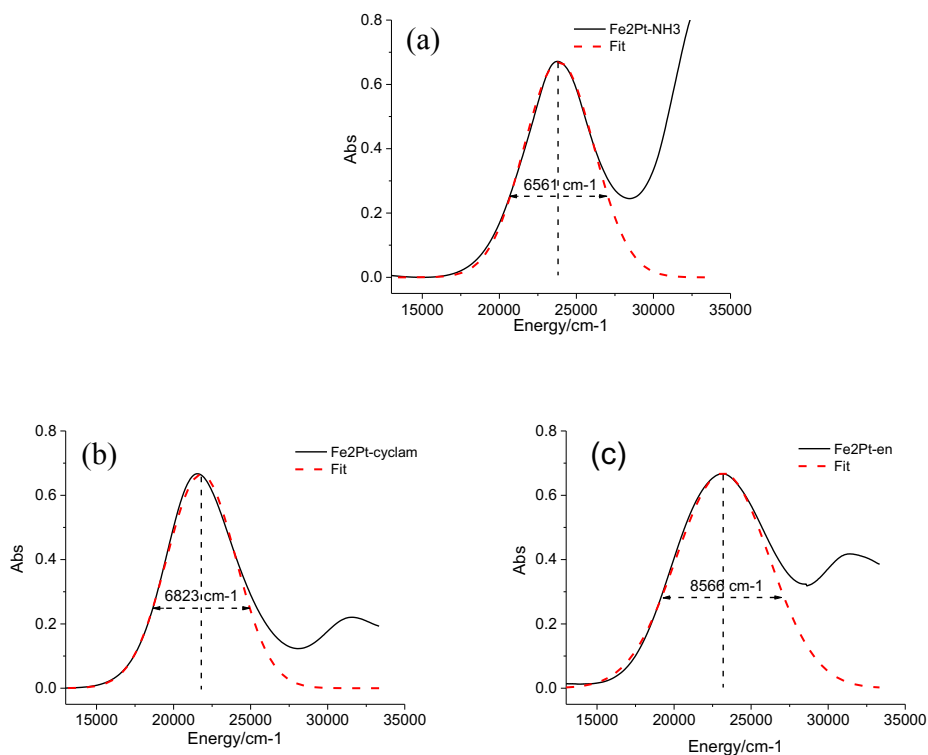


Figure 1.4 UV-Vis spectra of $[\text{Fe}_2\text{Pt}(\text{NH}_3)_4]^{4+}$ (a), $[\text{Fe}_2\text{Pt}(\text{en})_2]^{4+}$ (b) and $[\text{Fe}_2\text{Pt}(\text{cyclam})]^{4+}$ (c) showing Gaussian fits of lowest energy band

1.3.2 Raman and Resonance Raman Spectroscopy

The Raman and resonance Raman spectra were collected for all three complexes. For $[\text{Fe}_2\text{Pt}(\text{NH}_3)_4]^{4+}$, the following excitation wavelengths were used: 405 nm, 413 nm, 424 nm, 467 nm, 490 nm, 532 nm, 561 nm and 785 nm. For $[\text{Fe}_2\text{Pt}(\text{cyclam})]^{4+}$, the following excitation wavelengths were used: 412 nm, 420 nm, 431 nm, 439 nm, 451 nm, 461 nm, 482 nm, 491 nm, 532 nm, 561 nm, 785 nm. For $[\text{Fe}_2\text{Pt}(\text{en})_2]^{4+}$, the following excitation wavelengths were used: 410 nm, 420 nm, 436 nm, 448 nm, 470 nm, 532 nm, 561 nm, 785 nm. Before performing the intensity analysis, we corrected for self-absorption by using

the raw data to multiply the observed spectrum by $10^{A(\lambda)}$, where $A(\lambda)$ is the electronic absorption spectra of the complexes.¹²

Figure 1.4 contains the comparison of the resonance Raman spectra (@532 nm) and non-resonance Raman spectra (@785nm) of the three trinuclear complexes to show intensity enhancement. $[\text{Fe}_2\text{Pt}(\text{NH}_3)_4]^{4+}$ spectra was normalized the integrate area of KNO_3 peak (1047.3 cm^{-1}). $[\text{Fe}_2\text{Pt-cyclam}]^{4+}$ and $[\text{Fe}_2\text{Pt}(\text{en})_2]^{4+}$ were normalized to the integrate area of K_2SO_4 peak (979.8 cm^{-1}). The comparison of the corrected Raman spectra of $[\text{Fe}_2\text{Pt}(\text{NH}_3)_4]^{4+}$, $[\text{Fe}_2\text{Pt-cyclam}]^{4+}$ and $[\text{Fe}_2\text{Pt}(\text{en})_2]^{4+}$ collected using 532 nm laser excitation is shown in Figure 1.6. The observed vibrational bands are assigned by analogy to previously reported complexes.^{10, 13}

The Raman frequency shifts (cm^{-1}) and vibrational modes assignment for each complexes is presented in Table 1.1. Table 1.2 contains the *relative* integrated intensities of these modes and the corresponding set of *absolute* displacements, Δ 's. The displacements were obtained using Savin's formula (eq. 1) and are scaled to match the width at the $(1/e)$ of the maximum of the absorption spectrum of each complex according to eq 2. In order to illustrate the difference in peak positions of the different modes compared to the absorption spectrum, the excitation profiles for each resonantly enhanced vibrational mode in Table 1.2 of those three trinuclear complexes overlaid with their electronic absorption spectrum are shown in Figure 1.7, Figure 1.8 and Figure 1.9, respectively.

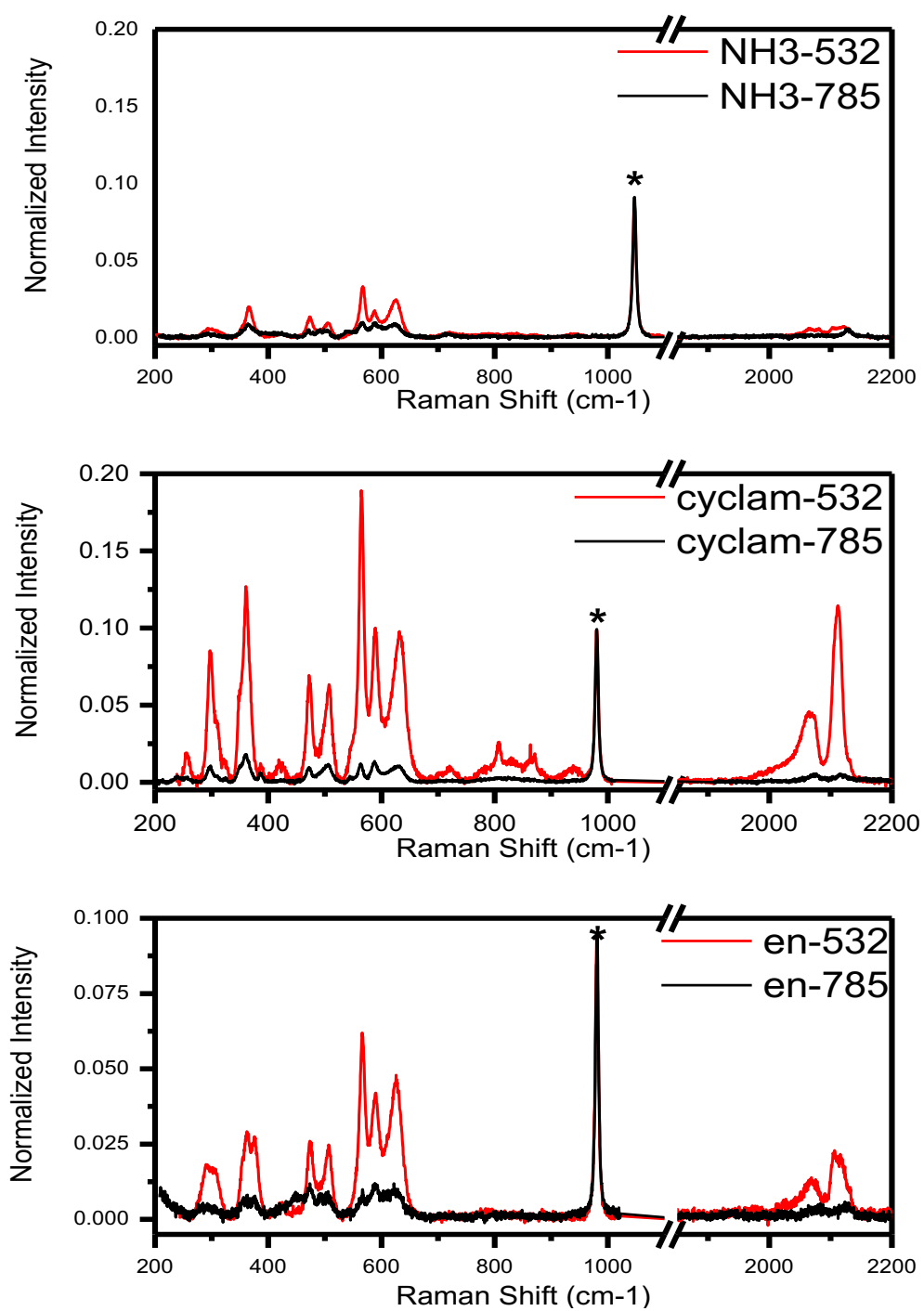


Figure 1.5 Resonance Raman spectra vs Non-resonance Raman spectra of [Fe₂Pt-(NH₃)₄]⁴⁺, [Fe₂Pt-(en)₂]⁴⁺, [Fe₂Pt-cyclam]⁴⁺

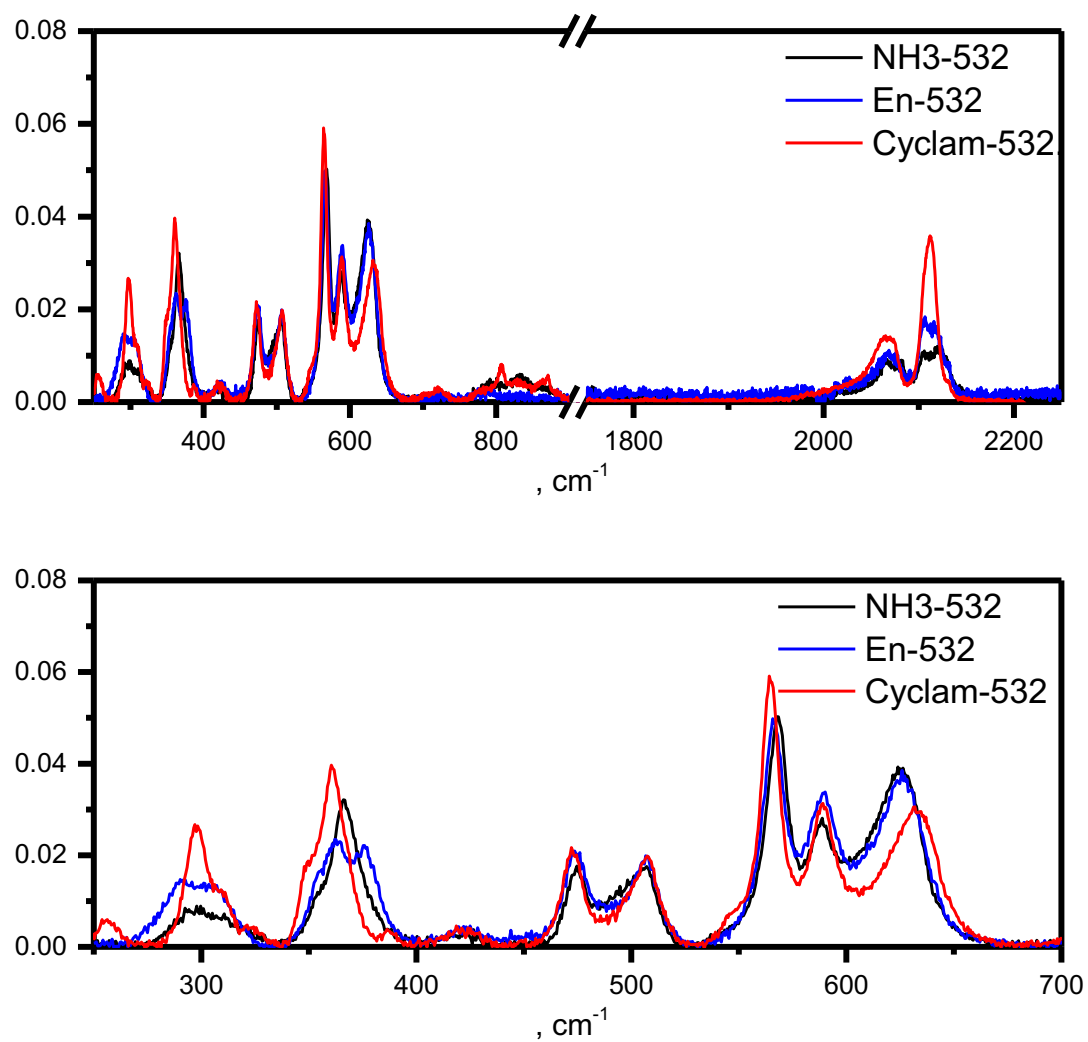


Figure 1.6 Raman spectrum of $[\text{Fe}_2\text{Pt}(\text{NH}_3)_4]^{4+}$ (black), $[\text{Fe}_2\text{Pt}(\text{en})_2]^{4+}$ (red) and $[\text{Fe}_2\text{Pt-cyclam}]^{4+}$ (blue)

Table 1.1 Raman shifts and Assignments of $[\text{Fe}_2\text{Pt}(\text{NH}_3)_4]^{4+}$, $[\text{Fe}_2\text{Pt}(\text{en})_2]^{4+}$ and $[\text{Fe}_2\text{Pt-cyclam}]^{4+}$

Fe₂Pt-NH₃	Fe₂Pt-en	Fe₂Pt-cyclam	Assignment^{10, 13}
		256.3	
298.5	291.3	298.8	δ (Pt-L*)
366.2	362.7	360.5	ν (Pt-NC)-bridge
421.8	423.2	421.6	δ (Fe-CN)
472.8	474.2	472.7	δ (Fe-CN)
507.1	506.7	508.1	ν (Pt-L*)
568.4	566.3	564.2	ν (Fe-CN)-
588.7	589.5	589.1	ν (Fe-CN)-radial
626.2	625.9	631.8	ν (Fe-CN)-axial
2064.9	2064.0	2064.2	ν (CN)-radial
2080.2	2074.7	2079.0	ν (CN)-radial
2105.7	2105.2	2105.3	ν (NC)-axial
2122.3	2117.2	2114.9	ν (CN)-bridge

* *L* corresponds to NH_3 , *en*, or *cyclam*; ν stretching mode, δ bending mode.

Table 1.2 Raman Data and Intensity Analysis Calculations of $[\text{Fe}_2\text{Pt}(\text{NH}_3)_4]^{4-}$, $[\text{Fe}_2\text{Pt}(\text{en})_2]^{4-}$ and $[\text{Fe}_2\text{Pt-cyclam}]^{4-}$

Fe2Pt-NH3			Fe2Pt-en			Fe2Pt-cyclam		
ν (cm^{-1})	Intensity	Δ	ν (cm^{-1})	Intensity	Δ	ν (cm^{-1})	Intensity	Δ
						256.3	0.16	1.99
298.5	0.98	3.59	291.3	0.61	4.28	298.8	0.80	3.87
			305.3	0.39	3.23			
366.2	1.87	4.04	362.7	0.77	3.85	360.5	1.56	4.49
			375.9	0.59	3.23			
421.8	0.32	1.44	423.2	0.11	1.27	421.6	0.13	1.12
472.8	0.87	2.13	474.2	0.60	2.59	472.7	0.56	2.06
507.1	0.99	2.12	506.7	0.71	2.65	508.1	0.83	2.33
568.4	2.14	2.78	566.3	1.42	3.34	564.2	1.48	2.79
588.7	1	1.83	589.5	1	2.70	589.1	1	2.20
626.2	4.04	3.46	625.9	2.57	4.08	631.8	2.15	3.01
2064.9	0.62	<i>b</i>	2064.0	0.36	<i>b</i>	2064.2	0.89	<i>b</i>
2080.2	0.29	<i>b</i>	2074.7	0.29	<i>b</i>	2079.0	0.18	<i>b</i>
2105.7	0.43	0.34	2105.2	0.38	0.47	2105.3	0.78	0.54
2122.3	0.79	0.45	2117.2	0.66	0.61	2114.9	0.60	0.47

^b Because these modes have been identified as non-totally symmetric (ie. not expected to significantly contribute to the width of the absorption spectrum), we did not calculate the relative displacement using the simple intensity approach described in the text.¹¹

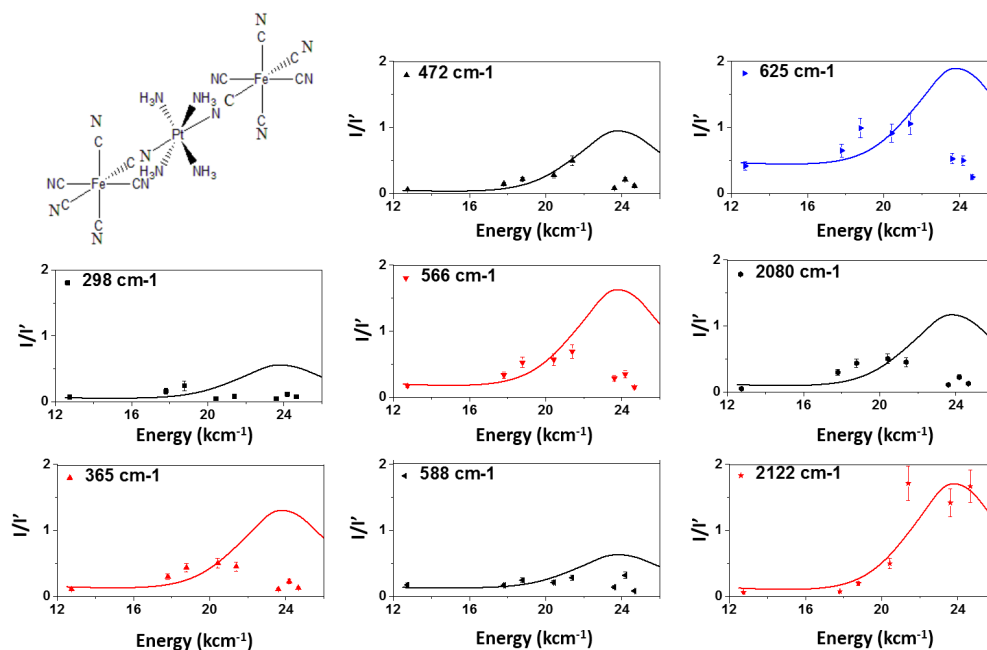


Figure 1.7 Resonance Raman excitation profile data points (see text for excitation wavelengths used) overlaid with the scaled absorption spectrum of $[\text{Fe}_2\text{Pt}(\text{NH}_3)_4]^{4-}$

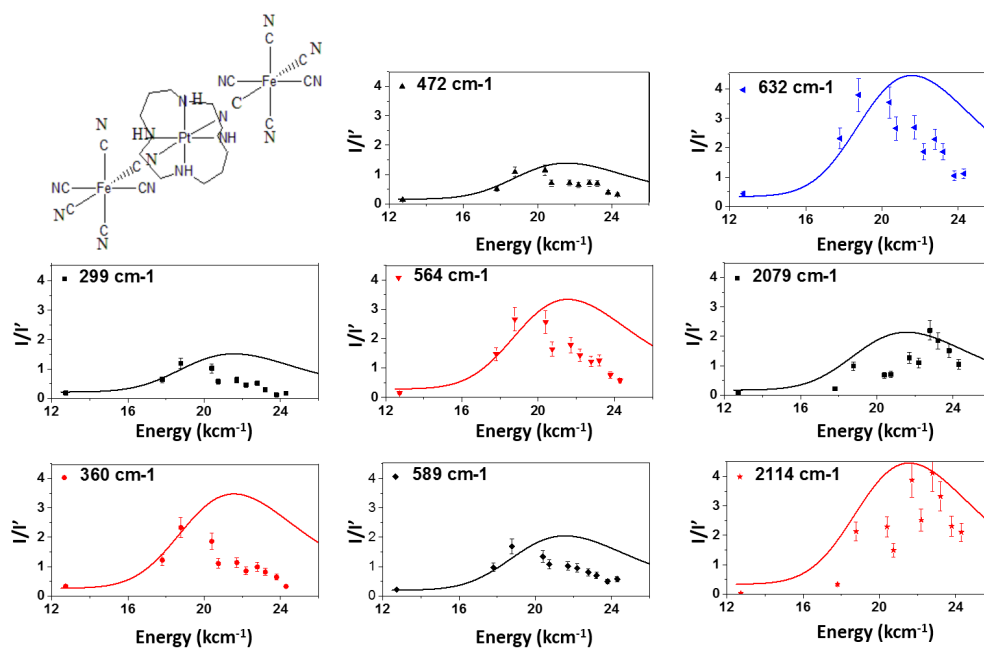


Figure 1.8 Resonance Raman excitation profile data points (see text for excitation wavelengths used) overlaid with the scaled absorption spectrum of $[\text{Fe}_2\text{Pt-cyclam}]^{4-}$

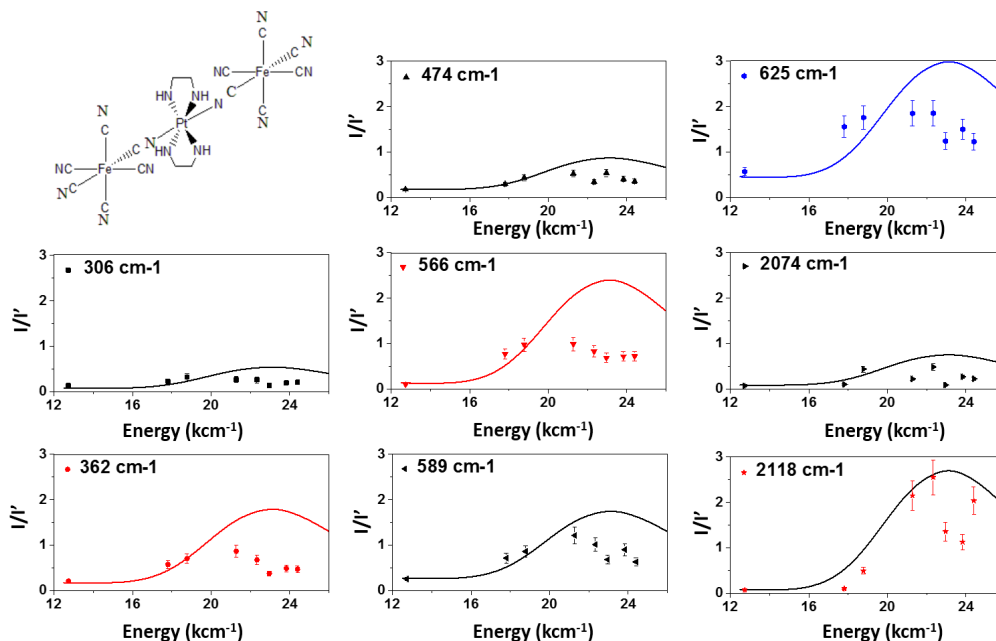


Figure 1.9 Resonance Raman excitation profile data points (see text for excitation wavelengths used) overlaid with the scaled absorption spectrum of $[\text{Fe}_2\text{Pt}(\text{en})_2]^{4-}$

1.4 Discussion

Raman frequencies and relative displacements are summarized in Table 1.1 and Table 1.2. Based on the frequencies shifts observed for each complex we can predict the degree of delocalization of electron density in the ground state of the complexes, which is dictated by orbital overlap and conformation of the complex. The most important modes that allow analysis are the bridging ones. They are the most affected by the orbital overlap between the metal centers. From the comparison of $[\text{Fe}_2\text{Pt}(\text{cyclam})]^{4-}$ and $[\text{Fe}_2\text{Pt}(\text{NH}_3)_4]^{4-}$ complexes we can see that, the $\nu(\text{Pt}-\text{NC})$ -bridge, $\nu(\text{CN})$ -bridge and $\nu(\text{Fe}-\text{CN})$ -bridge modes of $\text{Fe}_2\text{Pt}(\text{cyclam})^{4-}$ shifted to lower energy by 5.7 cm^{-1} , 4.2 cm^{-1} and 5.7 cm^{-1} , respectively, compared with $[\text{Fe}_2\text{Pt}(\text{NH}_3)_4]^{4-}$ complex. On the other hand, the $\nu(\text{Fe}-$

CN)-axial mode is shifted by 5.6 cm^{-1} to higher energy for $\text{Fe}_2\text{Pt-cyclam}^{4+}$ complex compared to the analogous mode of $[\text{Fe}_2\text{Pt}(\text{NH}_3)_4]^{4+}$.

We hypothesize that the changes in M-L stretching frequencies involving the cyano groups indicate a higher degree of electron delocalization in the ground state for the cyclam complex. Cyanide is strong field ligand and has strong π -backbonding. Both complexes experience π -backbonding from the Fe to the CN bridge but in the case of $[\text{Fe}_2\text{Pt-cyclam}]^{4+}$, shift of the electron density to the Pt center would lead to weaker bridging Fe-C bond compare to that $[\text{Fe}_2\text{Pt}(\text{NH}_3)_4]^{4+}$ complex.¹⁴ Smaller Pt-NC stretch is caused by lower charge on the Pt center due to the same reason. By comparing the bridging modes frequencies we can conclude that the eclipsed conformation allows more electronic delocalization across the Fe-CN-Pt bridge due to resonance effect. This point is illustrated by the simplified bonding picture depicted in Figure 1.10. The ν (Fe-CN)-axial mode is shifted by 5.6 cm^{-1} to higher energy for $[\text{Fe}_2\text{Pt-cyclam}]^{4+}$ compared to this mode in $[\text{Fe}_2\text{Pt}(\text{NH}_3)_4]^{4+}$. This indicates a smaller force constant for Fe-CN in $[\text{Fe}_2\text{Pt}(\text{NH}_3)_4]^{4+}$ complex, because there is more electron density localized in Fe-CN bridge bond, which leads to less electron density in Fe-CN axial bond, and this make Fe-CN axial bond weaker in $[\text{Fe}_2\text{Pt}(\text{NH}_3)_4]^{4+}$ complex.

Figure 1.6 is the overlay Raman spectrum of those three complexes at 532 nm. From the spectrum we can see that $[\text{Fe}_2\text{Pt}(\text{en})_2]^{4+}$ has all the modes have frequencies that are in between those of $[\text{Fe}_2\text{Pt-cyclam}]^{4+}$ and $[\text{Fe}_2\text{Pt-NH}_3]^{4+}$. Therefore we can conclude that conformation should be in between staggered and eclipsed. The only difference for

$[\text{Fe}_2\text{Pt}(\text{en})_2]^{4+}$ compared to the rest two is presence of 375.9 cm^{-1} peak, which may be explained either by presence of second conformation which decreased overlap compared by complexes with other ligands, or due to presence of ethylenediamine modes which overlap with Pt-NC bridging mode.

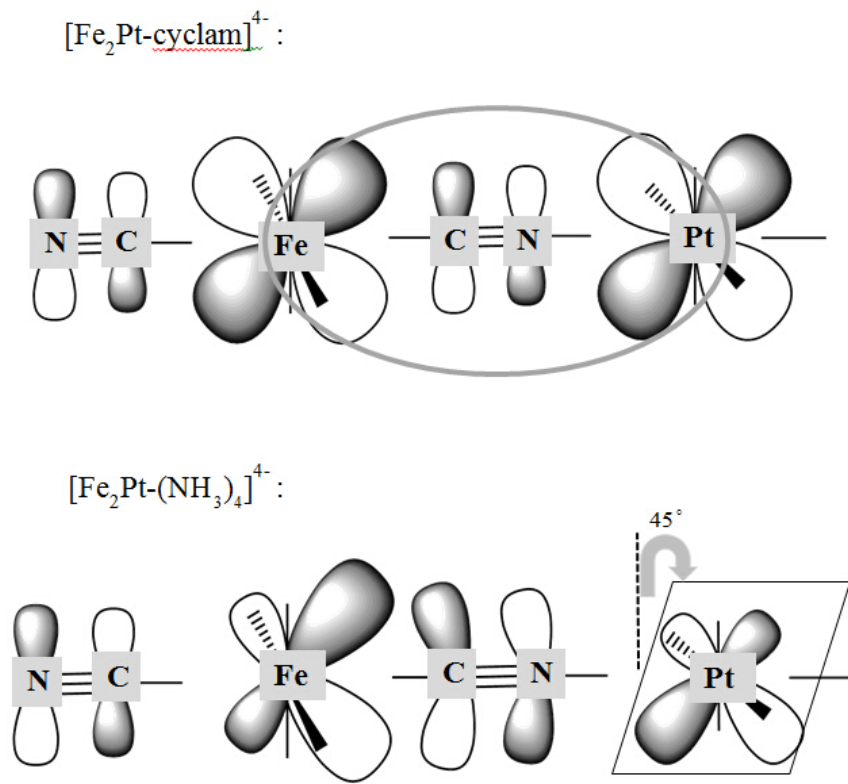


Figure 1.10 Simplified bonding illustration of $[\text{Fe}_2\text{Pt-cyclam}]^{4+}$ (up) vs $[\text{Fe}_2\text{Pt}(\text{NH}_3)_4]^{4+}$ (down)

The Raman intensity analysis was carried out to determine the structure changes associated with the (MMCT) charge transfer excited state. The displacements obtained for the $[\text{Fe}_2\text{Pt}(\text{NH}_3)_4]^{4+}$ complex (list in Table 1.2) was closely match those previously reported for this complex.¹⁰ From Table 2, we can see that the vibrational modes related

to the Fe-CN-Pt bridge for both of these two complexes have the biggest relative displacements. This indicates that the largest contributions to the vibrational barrier to electron transfer were those modes associated with the Fe-CN-Pt bridge in both cases. From the excitation profiles we can see that for each complexes, the vibrational modes which are related with Fe-Pt-Fe bridge (red), have relative higher enhancements. The $\nu(\text{Fe-CN})$ -axial modes for each complexes (blue) also have higher relative intensity. Those relative higher enhancements mean they have larger distortions.

1.5 References

1. White, J. L.; Baruch, M. F.; Pander, J. E., III; Hu, Y.; Fortmeyer, I. C.; Park, J. E.; Zhang, T.; Liao, K.; Gu, J.; Yan, Y.; Shaw, T. W.; Abelev, E.; Bocarsly, A. B., *Chem. Rev. (Washington, DC, U. S.)* **2015**, *115* (23), 12888-12935.
2. Chaurasia, S.; Lin, J. T., *Chem. Rec.* **2016**, *16* (3), 1311-1336.
3. Park, H.; Kim, H.-i.; Moon, G.-h.; Choi, W., *Energy Environ. Sci.* **2016**, *9* (2), 411-433.
4. Dereka, B.; Koch, M.; Vauthey, E., *Acc. Chem. Res.* **2017**, *50* (2), 426-434.
5. O'Neill, M. A.; Becker, H. C.; Wan, C.; Barton, J. K.; Zewail, A. H., *Angewandte Chemie* **2003**, *115* (47), 6076-6080.
6. Spitler, E. L.; Haley, M. M., *Tetrahedron* **2008**, *64* (50), 11469-11474.
7. Chattopadhyay, S.; Jana, P.; Mitra, A.; Sarkar, S.; Ganguly, T.; Mallick, P., *Journal of Raman spectroscopy* **1997**, *28* (8), 559-565.
8. Sett, P.; Misra, T.; Chattopadhyay, S.; De, A.; Mallick, P., *Vibrational spectroscopy* **2007**, *44* (2), 331-342.
9. Lochbrunner, S.; Szeghalmi, A.; Stock, K.; Schmitt, M., *The Journal of chemical physics* **2005**, *122* (24), 244315.
10. Pfennig, B. W.; Wu, Y.; Kumble, R.; Spiro, T. G.; Bocarsly, A. B., *The Journal of Physical Chemistry* **1996**, *100* (14), 5745-5750.
11. Doorn, S. K.; Blackbourn, R. L.; Johnson, C. S.; Hupp, J. T., *Electrochimica acta* **1991**, *36* (11-12), 1775-1785.
12. Streckas, T. C.; Adams, D. H.; Packer, A.; Spiro, T. G., *Applied Spectroscopy* **1974**, *28* (4), 324-327.

13. Doorn, S. K.; Hupp, J. T., *Journal of the American Chemical Society* **1989**, *111* (3), 1142-1144.
14. Korzeniewski, C.; Severson, M.; Schmidt, P.; Pons, S.; Fleischmann, M., *Journal of Physical Chemistry* **1987**, *91* (22), 5568-5573.

Chapter Two

Resonance Raman Spectroscopy Study of Cu(I) Complexes

2.1 Introduction

Transition metal coordination complexes have wide range applications from solar energy materials to chemical sensors.¹⁻² To make these applications economical and viable, much attention is being focused on first-row transition-metal-based system. Copper(I) diimine coordination complexes have been of interest for numbers of years.³⁻⁵ After populating through photoexcitation, those copper(I) complexes have the ability to flatten out in the metal-to-ligand charge transfer (MLCT) state. This ability is crucial to the subsequent dynamics and structures present in the excited state.⁶⁻⁷

Resonance Raman is a technique can give us some information about the structural distortions between ground state and excited state. It is possible to use Raman intensity analysis to determine the relative displacements of the vibrational modes in excited state. Our collaborator Dr. Karen Mulfort of Argonne National Laboratory has synthesized a series of Cu(I) complexes. They have different ligand environments, one Cu(I) dimer complex and three Cu(I) monomers. Figure 2.1 is the structures of Cu(I)- monomers and Cu(I)-dimer . We propose to use resonance Raman to investigate how the coupling of two Cu(I) atoms through a bridging bisphenanthroline ligand affects the nature of the MLCT excited state.

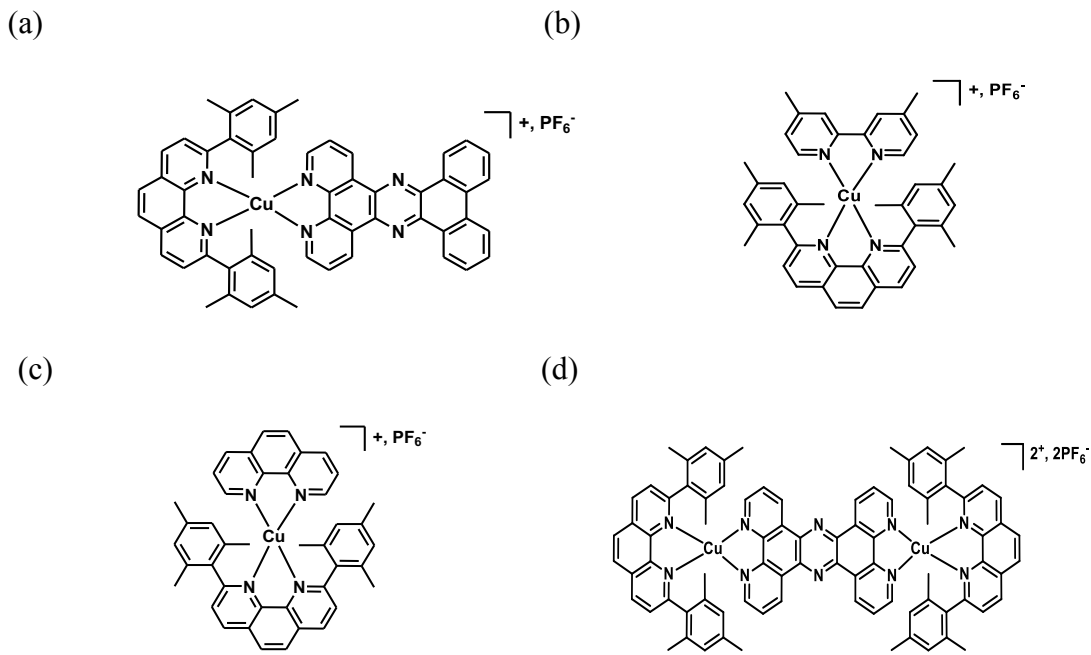


Figure 2.1 Structures of Cu(I) complexes: (a) Cu(I)-monomer-1; (b) Cu(I)-monomer-2;
(c) Cu(I)-monomer-3; (d) Cu(I)-dimer

2.2 Methods

2.2.1 UV-Vis Spectroscopy

Ultraviolet-visible spectroscopy refers to absorption spectroscopy in the ultraviolet-visible spectral region. UV-vis spectra of the samples were obtained in the CH_3CN solution containing 5 mM of each complex, in a quartz cuvette with 10 mm pathlength, using a Cary-Varian UV-visible-NIR spectrophotometer.

2.2.2 Raman Spectroscopy

Normal Raman measurements were collected using the picosecond Ti: Sapphire oscillator tunable laser to generate the laser 705 nm laser with ~25 mW power; Resonance Raman were collected using 532 nm single-frequency solid state lasers. Spectra were collected using a triple monochromator, and a liquid nitrogen-cooled CCD detector with a 1340 × 100 pixel chip (Princeton Instruments). The sample was spun to minimize the residence time of the laser on one spot of the sample, to avoid excessive heating. The Raman data were collected in solid state tablet with 10 wt.% of KNO₃ as an internal standard, 80 wt. % of KBr and 10 wt. % of Cu(I) complex, respectively.

2.3 Results and Discussion

The UV-Vis absorption spectra of the four Cu(I) complexes are shown in Figure 2.2. The lower energy bands (peaks maxima around 475 nm) in the figure were assigned as metal-to-ligand charge transfer (MLCT). The Cu(I) dimer appears to be measurably red shifted compared to the monomers.

The Raman and resonance Raman spectra were collected for all four complexes with the excitation wavelengths at 705 nm and 532 nm, respectively. Figure 2.3, Figure 2.4, Figure 2.5 and Figure 2.6 contain the comparison of the Raman spectra and resonance Raman spectra for each of those four complexes. All the spectra were normalized to the integrated area of the KNO₃ peak (1050.6 cm⁻¹).

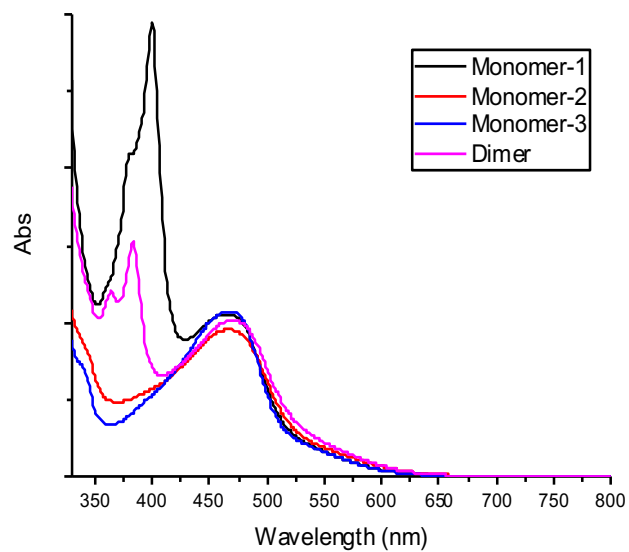


Figure 2.2 UV-Vis absorption spectrum of Cu(I) complexes

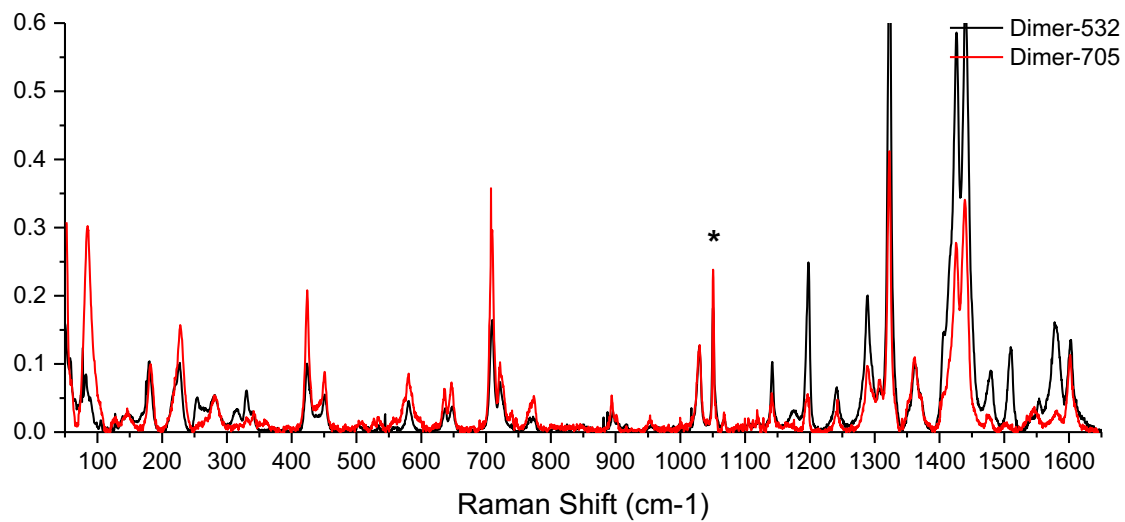


Figure 2.3 Raman and resonance Raman spectra of Cu(I) dimer

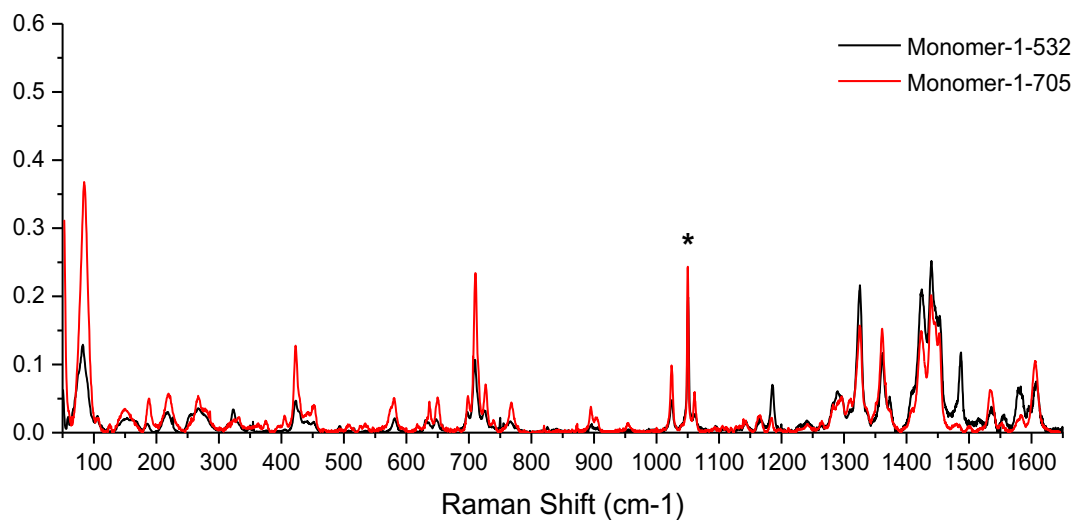


Figure 2.4 Raman and resonance Raman spectra of Cu(I) monomer-1

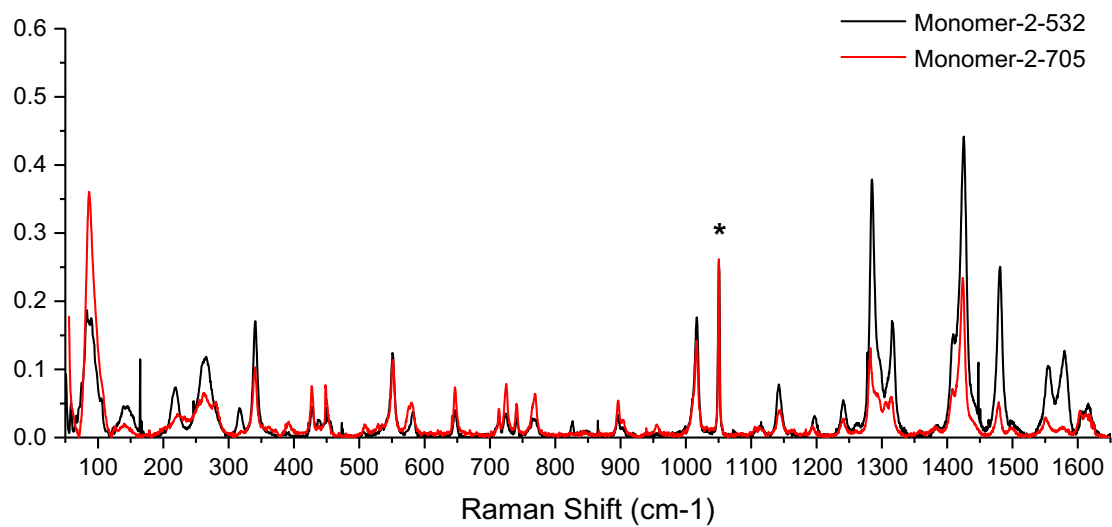


Figure 2.5 Raman and resonance Raman spectra of Cu(I) monomer-2

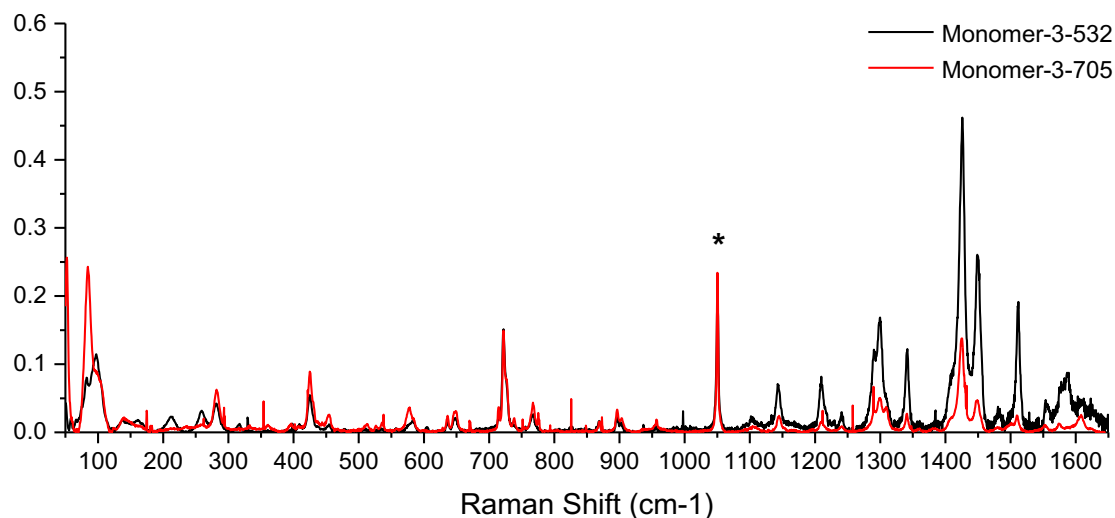


Figure 2.6 Raman and resonance Raman spectra of Cu(I) monomer-3

From the comparison of Raman and resonance Raman spectra of those four Cu(I) complexes, we observed that all of them have some enhancement modes at high wavenumber region between 1000 cm^{-1} and 1650 cm^{-1} . These modes are related to the ligand skeletal modes and structure deformations involving the C-H bonds.

Figure 2.6 is the overlay Raman spectrum (@ 532 nm) of those four complexes at high frequency region. The comparison of the resonance Raman spectra of those four complexes at high frequency region is shown in Figure 2.7. From the figure we can see that they all have the similar modes around 1400 cm^{-1} to 1460 cm^{-1} which could be assigned as the breathing mode of the phenanthroline rings in the complexes.⁶ The modes

around 1580 cm^{-1} to 1630 cm^{-1} were reported as the localized distortion of a single phenanthroline ligand.⁷

The selected modes and their normalized intensities are shown in Table 2.1. The intensities were normalized to the integrated area of KNO_3 peak.

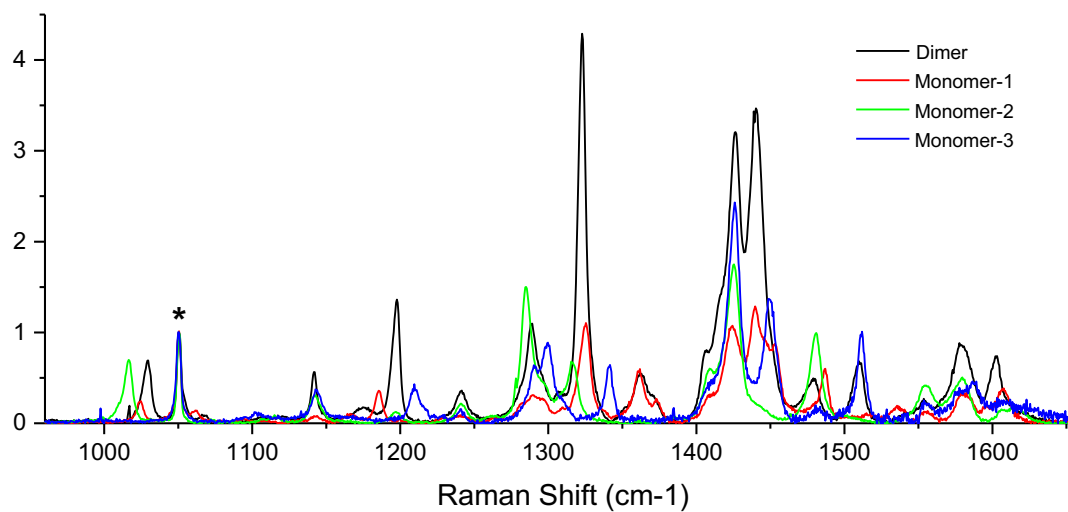


Figure 2.7 Resonance Raman spectra of Cu(I) dimer (black), monomer-1 (red), monomer-2 (green) and monomer-3 (blue)

Table 2.1 Raman frequency and intensity of Cu(I) Dimer, monomer-1, monomer-2 and monomer-3

Cu(I) Dimer		Cu(I) Monomer-1		Cu(I) Monomer-2		Cu(I) Monomer-3	
ν (cm ⁻¹)	Intensity						
81.9	0.45	81.9	0.65	85.0	0.68	97.5	0.60
1029.1	0.69	1024.8	0.24	1016.5	0.70		
1141.7	0.56	1144.3	0.07	1142.2	0.31	1143.3	0.36
1197.7	1.36	1185.3	0.36	1197.1	0.13	1209.5	0.43
1288.6	1.10	1290.2	0.31	1284.4	1.50	1299.7	0.89
1322.8	4.29	1325.4	1.10	1316.0	0.66	1341.6	0.64
1426.9	3.18	1423.8	1.07	1425.4	1.75	1425.9	2.43
1440.2	3.47	1453.0	0.88	1481.0	0.99	1449.4	1.36
1509.3	0.66	1486.6	0.59	1554.1	0.42	1511.9	1.01
1578.2	0.85	1579.6	0.32	1580.1	0.48	1577.7	0.39
1602.5	0.72	1606.6	0.37	1616.0	0.20	1587.6	0.44

2.4 References

1. Shaw, G. B.; Grant, C. D.; Shirota, H.; Castner, E. W.; Meyer, G. J.; Chen, L. X., *Journal of the American Chemical Society* **2007**, *129* (7), 2147-2160.
2. Thanasekaran, P.; Liao, R.-T.; Liu, Y.-H.; Rajendran, T.; Rajagopal, S.; Lu, K.-L., *Coordination chemistry reviews* **2005**, *249* (9), 1085-1110.
3. Kirchoff, J. R.; Gamache Jr, R. E.; Blaskie, M. W.; Del Paggio, A. A.; Lengel, R. K.; McMillin, D. R., *Inorganic Chemistry* **1983**, *22* (17), 2380-2384.
4. Sauvage, J.-P., *Science* **2001**, *291* (5511), 2105-2106.
5. Lind, S. J.; Gordon, K. C.; Waterland, M. R., *Journal of Raman Spectroscopy* **2008**, *39* (11), 1556-1567.
6. Ullrich, S.; Schultz, T.; Zgierski, M. Z.; Stolow, A., *Physical Chemistry Chemical Physics* **2004**, *6* (10), 2796-2801.
7. Feichtinger, D.; Plattner, D. A., *Chemistry-a European Journal* **2001**, *7* (3), 591-599.

Chapter Three

Fundamental Study of Ru-S bonding in a Series of Ru-S/SO Complexes

3.1 Introduction

Molecular photochromic compounds are those that transform between two forms of one chemical species by the absorption of electromagnetic radiation, where the two forms have different absorption spectra. There are wide applications in areas of study have been found of these photochromic compounds, ranging from chemical biology to materials science, such as anticancer complexes and optical information storage devices.^{1,2}

Certain ruthenium polypyridine sulfoxide complexes are photochromic.³ The photo-triggered isomerization of this kind of complexes were the transformations of sulfoxide from Ru-S to Ru-O bonded. This photo-induced isomerization dramatically changed the spectroscopic and electrochemical properties of the metal complexes.⁴ Our collaborator Dr. Jeffrey Rack's group from The University of New Mexico synthesized a series of Ru-S and Ru-SO complexes as illustrated in Figure 3.1. The ligand abbreviations are as follows: where bpy is 2,2'-bipyridyl; me-bim-*i*pr is 2-(isopropylsulfanylmethyl)-1H-benzimidazole; et-bim-*i*pr is 2-(2-isopropylsulfanylethyl)-1H-benzimidazole; et-bim-ph is 2-(2-phenylsulfanylethyl)-1H-benzimidazole; et-bim-ph-4F is 2-[2-(4-fluorophenyl)sulfanylethyl]-1H-benzimidazole; et-bim-ph-4OMe is 2-[2-(4-methoxyphenyl)sulfanylethyl]-1H-benzimidazole; me-bimSO-*i*pr is 2-

(isopropylsulfinylmethyl)-1H-benzimidazole; et-bimSO-ipr is 2-(2-isopropylsulfinylethyl)-1H-benzimidazole; et-bimSO-ph is 2-[2-(benzenesulfinyl)ethyl]-1H-benzimidazole; et-bimSO-ph-4F is 2-[2-(4-fluorophenyl)sulfinylethyl]-1H-benzimidazole; et-bimSO-ph-4OMe is 2-[2-(4-methoxyphenyl)sulfinylethyl]-1H-benzimidazole. Me-bim-ipr is 2-(2-isopropylsulfonylmethyl)-1H-benzimidazole; et-bim-ipr is 2-(2-isopropylsulfonylethyl)-1H-benzimidazole; et-bim-ph is 2-(2-phenylsulfonylethyl)-1H-benzimidazole, et-bimSO-ipr is 2-(2-isopropylsulfinylethyl)-1H-benzimidazole. Subtle structural modification has been observed to significantly affect isomerization in ruthenium sulfoxide photochromes ⁵, and was believed to involve differences in Ru-sulfoxide bond covalency.

X-ray absorption spectroscopy (XAS) is a powerful probe of the local geometric and electronic structure of a photoabsorber. ⁶⁻⁸ It has been applied extensively to metal containing systems, where the extended X-ray absorption fine structure (EXAFS) region is used to determine metal–ligand bond distances and coordination numbers, and the edge region is used to obtain electronic structure information. In the case of S K-edge X-ray absorption spectra, these features occur due to electric-dipole-allowed transitions from the S 1s to 3p orbital which mix into the metal d orbitals due to bonding. Since the transitions under consideration are localized on the S atom, the pre-edge intensity reflects the amount of S character in these partially occupied or unoccupied metal d orbitals and thus the metal-S covalency. This methodology has been applied to various systems with metal-S bonds, and the S characters in the ground-state wave functions have been

successfully determined, making S K-edge X-ray absorption spectroscopy (XAS) a powerful spectroscopic technique.⁹

In our project, intermediate-energy X-ray absorption spectroscopy (XAS) was used to characterize the series of Ru-S/SO complexes related to their photochromic analogues. By collecting sulfur K-edge XAS data for this series of structurally similar complexes exhibiting diverse photochemical reactivity, and combine with TD-DFT calculations, the σ and π contributions to the HOMO may be characterized and correlated with their reactivity.

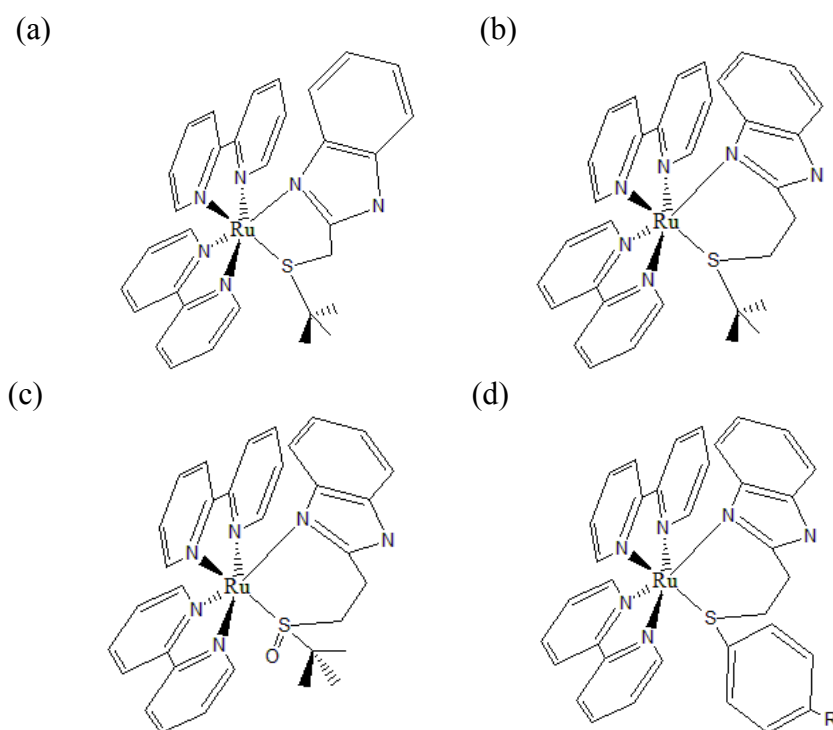


Figure 3.1 Structures of Ru-S complexes (a) me-bim-ipur; (b) et-bim-ipur; (c) et-bimSO-ipur; (d) et-bim-ph-R (R=H, R=MeO, R=F)

3.2 Methods

3.2.1 XAS Data collection

X-ray absorption data were collected at Advanced Photon Source (APS) in Argonne National Laboratory at 9-BM beamline in fluorescence mode at room temperature. The X-ray energy from Si (111) monochromator was calibrated relative to the 3% sodium thiosulfate standard. Three scans were collected in order to confirm the absence of X-ray damage and improve the signal-to-noise ratio. The spectra were processed and averaged in the Athena XAS analysis program.¹⁰

3.2.2 TD-DFT Calculations

To better understand these spectral trends, TD-DFT calculations were performed to provide a better idea of the orbital parentage of the underlying transitions.¹¹ All XAS calculations were performed using the ORCA quantum chemistry software package.¹² The PBE0 functional was utilized with the “def2-TZVP” basis set on all atoms excluding Ru, which was used “ZORA-TZVPP”. The optimized geometry structures were obtained from Dr. Charles Webster’s group in Mississippi State University. After the ground state DFT calculation, the sulfur 1s orbitals were localized using the Pipek-Mezey criteria and TD-DFT calculations were performed, allowing only for excitations from the localized sulfur 1s orbitals. Constant shift of +37.07 eV is required for this regime of basis sets to align calculated and experimental data. A 1.3 eV broadening was applied to all calculated absorption spectra.

3.3 Results and Discussion

We obtained the series of Ru-S complexes from Dr. Jeffrey Rack's group, The University of New Mexico. All XAS data were collected at APS in Argonne National Laboratory (Figure 3.2). The edge energy positions of the S and SO groups of complexes are consistent with the different effective oxidation state of the S in each case. Within each group of spectra, subtle differences in shape and relative intensity are observed. We chose four samples: me-bim-*i*-pr, et-bim-*i*-pr, et-bimSO-*i*-pr and et-bim-ph to run the TD-DFT calculations. The calculated spectra are contrasted with the experimental data in Figure 3.3 and show reasonable agreement.

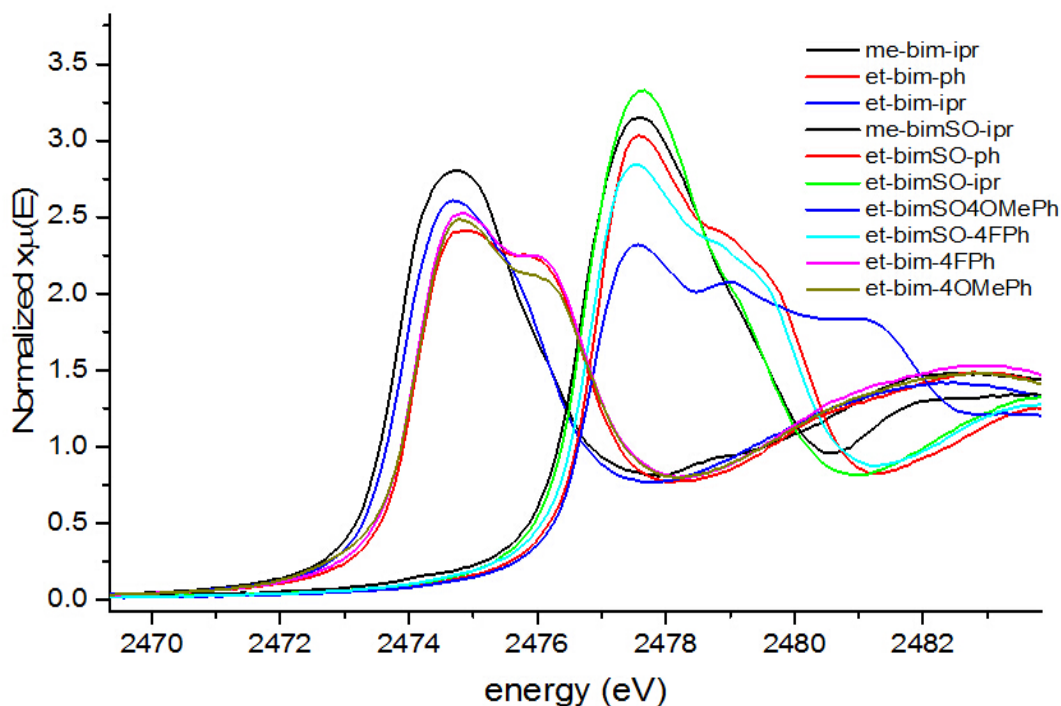


Figure 3.2 Experimental XAS spectrum of Ru-S/SO complexes

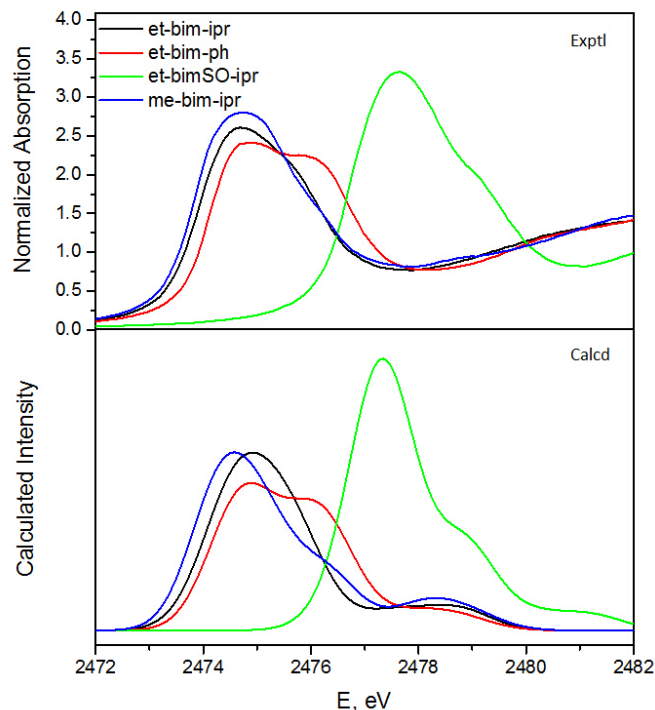


Figure 3.3 Comparison of the experimental (top) and calculated (bottom) S K-pre-edge spectra for Ru-S complexes. Calculated intensity in arbitrary units.

3.3.1 Me-bim-iph (A) vs Et-bim-iph (B):

Figure 3.4 is the calculated spectra of me-bim-iph(A, blue) and et-bim-iph(B, black). From the spectra, we can see that et-bim-iph shifted to higher energy compare with me-bim-iph. From the calculated results based on the molecular orbitals, we found that this shift is because that, in me-bim-iph, the first two transitions (red circles) have relative higher intensity, and combine with the orbital graphs, those transitions are all related with the bipyridyl sides. Table 3.1 is the comparison of bond lengths and angles of those two samples. From the table we can find that the bond length of Ru-S and S-C of those two samples are basically same, the angle of me-S-Ru is 97.94° and in et-bim-iph complex,

the angle of et-S-Ru 109.27° , we are surmising that it might be because smaller angle leads to easier transitions, which give higher intensity.

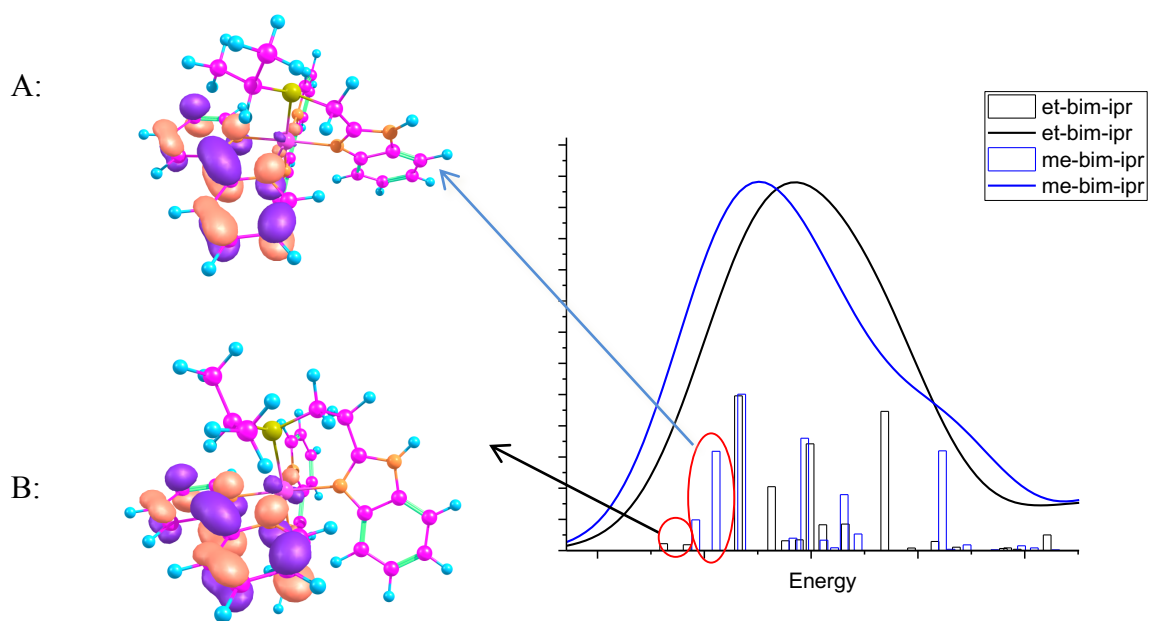


Figure 3.4 Calculated XAS spectrum of me-bim-ibr(blue) and et-bim-ibr(red)

Table 3.1 Calculated angle and bond length of me-bim-ibr vs et-bim-ibr

	Ru-S-C °	Ru-S (Å)	S-C(Å)
me-bim-ibr	97.94 °	2.39	1.84
et-bim-ibr	109.27 °	2.38	1.83

3.3.2 Et-bim-ph (A) vs Et-bim-ipr (B):

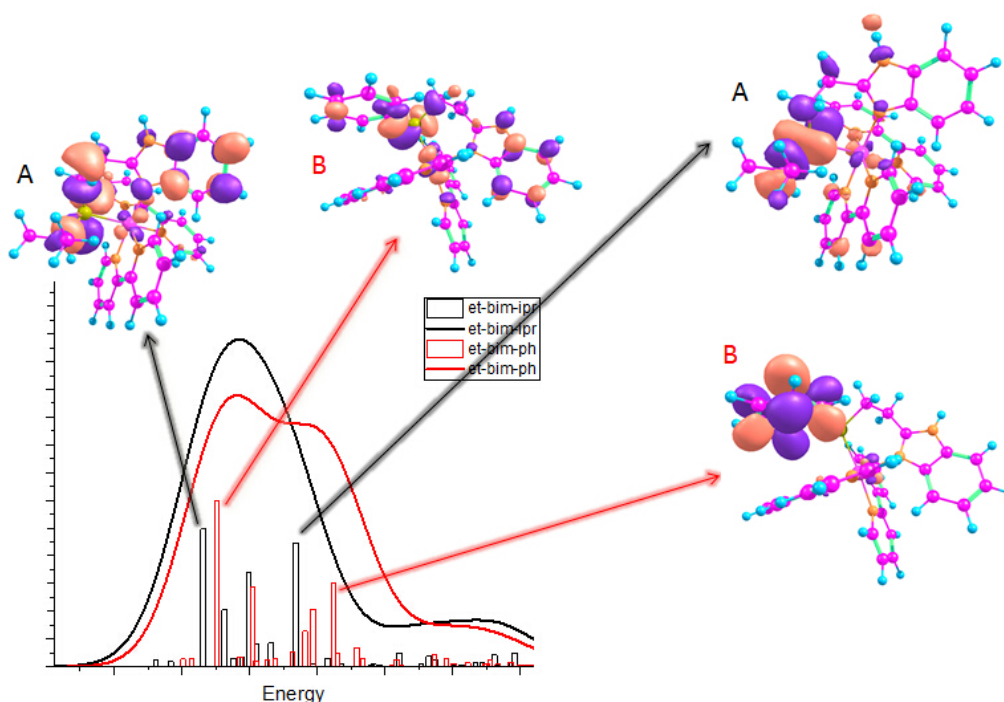


Figure 3.5 Calculated XAS spectrum of et-bim-ph(red) and et-bim-ipr(black)

Figure 3.5 is the calculated XAS spectrum of et-bim-ipr (A, black) and et-bim-ph (B, red). We can see that the spectrum of et-bim-ph has a shoulder at 2476.5 eV, which is match with our experimental spectrum. By analysis with our calculated results, from the molecular orbitals we can see that, the shoulder is due to the transition for S 1s orbital to the p orbitals of the carbons in benzene ring.

In this project, our main purpose was use XAS technique as a probe of the sulfur 1s \rightarrow 3p transition, when the sulfur ligand is bound to an open shell metal ion Ru^{2+} . The intensity

of this transition is tied to the amount of ligand p character in the metal d orbitals, and therefore the metal- ligand bond covalency. Based on our calculate results, we found that this transition is buried in the spectra, we could not see the feature from the experimental results. And we were unable to do the intensity analysis because of this issue. Also by comparing with other similar works that have been reported, we found this type of transition should show up at the lowest energy in the pre-edge region of the sulfur K-edge X-ray absorption spectrum.^{13,14}

3.4 References

1. Stiefel, E. I.; Brown, G. F., *Inorganic Chemistry* **1972**, *11* (2), 434-436.
2. Kelland, L., *Nature Reviews Cancer* **2007**, *7* (8), 573-584.
3. King, A. W.; Wang, L.; Rack, J. J., *Accounts of chemical research* **2015**, *48* (4), 1115-1122.
4. Rack, J. J., *Coordination Chemistry Reviews* **2009**, *253* (1), 78-85.
5. Rack, J. J.; Winkler, J. R.; Gray, H. B., *Journal of the American Chemical Society* **2001**, *123* (10), 2432-2433.
6. Roe, A.; Schneider, D.; Mayer, R.; Pyrz, J.; Widom, J.; Que Jr, L., *Journal of the American Chemical Society* **1984**, *106* (6), 1676-1681.
7. Lee, N.; Petrenko, T.; Bergmann, U.; Neese, F.; DeBeer, S., *Journal of the American Chemical Society* **2010**, *132* (28), 9715-9727.
8. Ümit, İ.; Dumoulin, F.; Sorokin, A. B.; Ahsen, V., *Turkish Journal of Chemistry* **2014**, *38*, 923-949.
9. Kelly, T. R.; Cai, X.; Damkaci, F.; Panicker, S. B.; Tu, B.; Bushell, S. M.; Cornella, I.; Piggott, M. J.; Salives, R.; Cavero, M., *Journal of the American Chemical Society* **2007**, *129* (2), 376-386.
10. Ravel, B.; Newville, M., *Journal of synchrotron radiation* **2005**, *12* (4), 537-541.
11. George, S. D.; Petrenko, T.; Neese, F., *Inorganica Chimica Acta* **2008**, *361* (4), 965-972.
12. Neese, F., Petrenko, T.; Ganyushin, D.; Olbrich G., *Coordination Chemistry Reviews* **2007**, *251*, 288- 327.

13. Sriskandakumar, T.; Behyan, S.; Habtemariam, A.; Sadler, P. J.; Kennepohl, P., *Inorganic chemistry* **2015**, *54* (23), 11574-11580.
14. Sriskandakumar, T.; Petzold, H.; Bruijninx, P. C.; Habtemariam, A.; Sadler, P. J.; Kennepohl, P., *Journal of the American Chemical Society* **2009**, *131* (37), 13355-13361.